Durability Improvement of Breeze-Driven Triboelectric-Electromagnetic Hybrid Nanogenerator by a Travel-Controlled Approach

Yingjin Luo, Pengfei Chen, Leo N. Y. Cao, Zijie Xu, Ying Wu, Gaofa He,* Tao Jiang,* and Zhong Lin Wang*

Triboelectric nanogenerator (TENG), as an emerging technology for distributed energy harvesting, provides a promising energy solution for self-powered environmental monitoring. However, the abrasion of triboelectric materials lowers the output performance of TENGs, severely limiting their practical applications. Herein, a novel travel-controlled approach, by combining a gear train and cam switch, is proposed to reduce the mechanical wear. The automatic switching between the contact and non-contact modes can be achieved in a tunable frequency, showing excellent electrical stability by maintaining 90% of electric outputs after continuous operation for 80 h (1 920 000 cycles). Meanwhile, based on the structural optimization, the power density per unit wind speed of the travel-controlled TENG (TC-TENG) is doubled as compared with that of previous related works. Moreover, by integrating the triboelectric-electromagnetic hybrid device with an energy management circuit, a self-powered close-looped environmental monitoring and alarming system are demonstrated. Under breezy conditions (below 3 m s^{-1}), the system can detect the environmental information continuously and steadily, and transmit it wirelessly to a mobile device. This work renders a novel approach to reducing the wear in TENGs toward self-powered wireless sensing systems, showing broad application prospects in distributed unmanned environmental monitoring, smart farming, and Internet of Things.

1. Introduction

With the rapid developments of Internet of Things (IoTs) and Big Data technologies, widely distributed sensors have been potentially used in a variety of sites, such as oceans, forests, and deserts.[1] Although most of these sensors do not require high power, their maintenance is very difficult when located in uninhabited areas for long-term purposes, because the batteries for the power supply need to be changed frequently.[2] Moreover, the produced battery waste can cause serious environmental pollution. Therefore, seeking an eco-friendly power supply technology by harvesting environmental energy has been considered a promising solution to the constraints of conventional power supply.[3] Wind energy, as one of the clean and renewable environmental energy sources, can serve as an outstanding solution to power distributed sensors, due to its advantages of high energy density and wide distribution.[4] To harvest wind energy, most traditional technologies, such as the electromagnetic generator (EMG), need to operate at wind speeds above 4 m s^{-1}.[5] However, the average wind speed at an observation altitude of 10 m is only 3.28 m s^{-1},[6] implying that conventional technologies are not suitable for breeze energy harvesting.

Triboelectric nanogenerator (travel-controlled TENG (TC-TENG), also called as Wang generator), invented by Wang and coworkers in 2012, is an effective approach for converting high-entropy mechanical energy (including breeze energy) into electricity.[7] Different from the EMG relying on Faraday's law

Y. Luo, P. Chen, L. N. Y. Cao, Z. Xu, T. Jiang, Z. L. Wang
CAS Center for Excellence in Nanoscience
Beijing Key Laboratory of Micro-Nano Energy and Sensor
Beijing Institute of Nanoenergy and Nanosystems
Chinese Academy of Sciences
Beijing 101400, P. R. China
E-mail: jiangtao@binn.cas.cn
Y. Luo, Y. Wu, G. He
School of Mechanical and Power Engineering
Chongqing University of Science & Technology
Chongqing 401331, P. R. China
E-mail: hegaofa@cqust.edu.cn

P. Chen, L. N. Y. Cao, Z. Xu, T. Jiang, Z. L. Wang
School of Nanoscience and Technology
University of Chinese Academy of Sciences
Beijing 100049, P. R. China
Z. L. Wang
School of Materials Science and Engineering
Georgia Institute of Technology
Atlanta, GA 30332-0245, USA
E-mail: zhong.wang@mse.gatech.edu

**ADVANCED
SCIENCE NEWS**
www.advancedsciencenews.com

**ADVANCED
FUNCTIONAL
MATERIALS**
www.afm-journal.de

of electromagnetic induction, the TENG, by coupling the triboelectrification and electrostatic induction, originated from Maxwell's displacement current.[8] Due to the unique advantages of low manufacturing costs, high voltage, and high-power density, the TENGs suit especially for harvesting low-frequency energies, including wind, water wave, and flow energies. And the further combination with the EMG can provide a promising strategy for broad frequency band energy harvesting with higher performance.[9]

Limited by the contact-separation nature of TENGs at two unique working modes, (i.e., lateral-sliding and contact-separation modes), the system friction and mechanical wear during the operation have always been obstacles restricting their performance.[10] At present, numerous approaches have been proposed to effectively reduce mechanical wear, such as triboelectric material optimization[11] and low-wear working mode.[12] In these works, the durability of the TENGs has been improved, but there are still problems in the standardization of fabrication and generality of methods. For example, a centrifugal method has been used to switch the devices from contact to non-contact mode at high wind speed, enhancing the stability and durability of TENG.[13] However, the current mode switching requires a disengagement speed over 300 rpm, making it only suitable for high wind speed scenarios. This means that these methods are difficult to adopt in real applications due to the strict requirements for the operating environment. Therefore, for the energy harvesting of low-speed wind, more general strategies need to be proposed to reduce dependence on the environment and increase the system's robustness while maintaining the desired power output.

In this work, we present a travel-controlled method using a tunable cam switch for stable and automatic mode transition to improve the stability and durability of the TENG (travel-controlled TENG, TC-TENG) for effectively harvesting breeze energy. An EMG is also hybridized with the TC-TENG to raise the overall electric outputs. The rotation of the wind cup not only drives the rotor of the hybrid generator unit to rotate, but also transmits the force to the cam switch through the gear train, to realize the periodic contact separation of the stator and rotor. The automatic switching between the contact and non-contact modes can be achieved at a low starting wind speed of 3 m s^{-1}, which can reduce the mechanical wear and thereby enhance the device durability. The electric outputs can maintain 90% of the initial values after a continuous operation of 80 h (total of 1.92 million cycles). Also, the influences of the structural parameters and external wind conditions on the device outputs were systematically studied. And through structural optimization, the power density per unit wind speed of the TC-TENG is doubled. Furthermore, combining the power management, the applications of powering the hygrothermographs through breeze energy harvesting were demonstrated toward self-powered intelligent environmental monitoring and alarming.

2. Results and Discussion

2.1. Structure and Working Principle of theHhybrid Device

The whole structure of the breeze-driven hybrid nanogenerator device containing the TC-TENG and EMG is schematically illustrated in **Figure 1**a, and the physical model is shown in Figure S1, Supporting Information. It consists of five main parts: wind cup, shell, transmission unit, cam switch, and hybrid generator unit. The transmission unit, made up of the drive shafts and transmission gear train, transmits a portion of the wind energy collected by the wind cup to the designed cam switch. During the rotation, the cam switch enables the switching between the contact mode and non-contact mode by lowering and raising the stator shaft height. The enlarged view of the hybrid generator unit is presented in Figure 1b. The rotor in acrylic material has two magnets of equal mass arranged symmetrically on the upper surface of the rotor and 15 fan-shaped polytetrafluoroethylene (PTFE) films with a central angle of 12° attached to the lower surface. Meanwhile, the stator in the same material with 30 nylon-coated copper electrodes with the same central angle attached to the upper surface of the stator and 4 copper coils in series evenly distributed on the lower surface. The detailed fabrication process of the rotor and stator can be found in the Experimental Section.

Figure 1c shows a schematic diagram of the automatic transition between the contact and non-contact modes for the TC-TENG, with the help of the cam switch. At the contact mode (upper part of Figure 1c), the protruding part (convex plate) of the cam switch holds up the stator to contact with the rotor by raising the drive shaft of the stator, which is connected to the linear bearing that slides along the longitudinal direction (Figure 1a). Under the rotational force from the wind cup, the cam switch continues to rotate until it reaches the end of the convex plate, and then the stator slides downwards under the action of the spring force of the reset spring and gravity. At this point, the contact mode changes to a non-contact mode, as shown in the lower part of Figure 1c. The mode switching requires no manual intervention as long as the wind cup keeps rotating. Furthermore, compared to the centrifugal force control method, the TC-TENG with optimized structural parameters can achieve a stable mode transition in light winds of 3 m s^{-1} (minimum 2 m s^{-1}). The switching time and separation height of the stator and rotor can be tuned by adjusting the length and height of the convex plate, respectively.

The operating principle of the TENG part is schematically shown in Figure 1d. It consists of an acrylic substrate (blue, green), PTFE film (pink), nylon film (cyan), and Cu electrodes (yellow, orange). The PTFE film slides between two adjacent Cu electrodes A (yellow) and B (orange) that are coated with nylon film. After several rounds of rubbing, the PTFE film obtains saturated negative charges due to the triboelectrification. When the PTFE film overlaps with electrode A (state i), the same amount of positive charges are generated on the nylon film surface. As the PTFE film slides from A to B, the electrons flow from electrode B to A across an external circuit to balance the change of potential difference (state ii). The induced current is produced from electrode A to B until the PTFE film fully overlaps with electrode B (state iii). When the PTFE film slides further (corresponding to the further rotation of the rotor), the electrons on electrode A flow back to electrode B (state iv), inducing an inverse current. With the relative rotation of the rotor and stator, the periodic charge transfer between electrodes A and B will produce alternating current and provide power to external loads, because of the periodic structure.
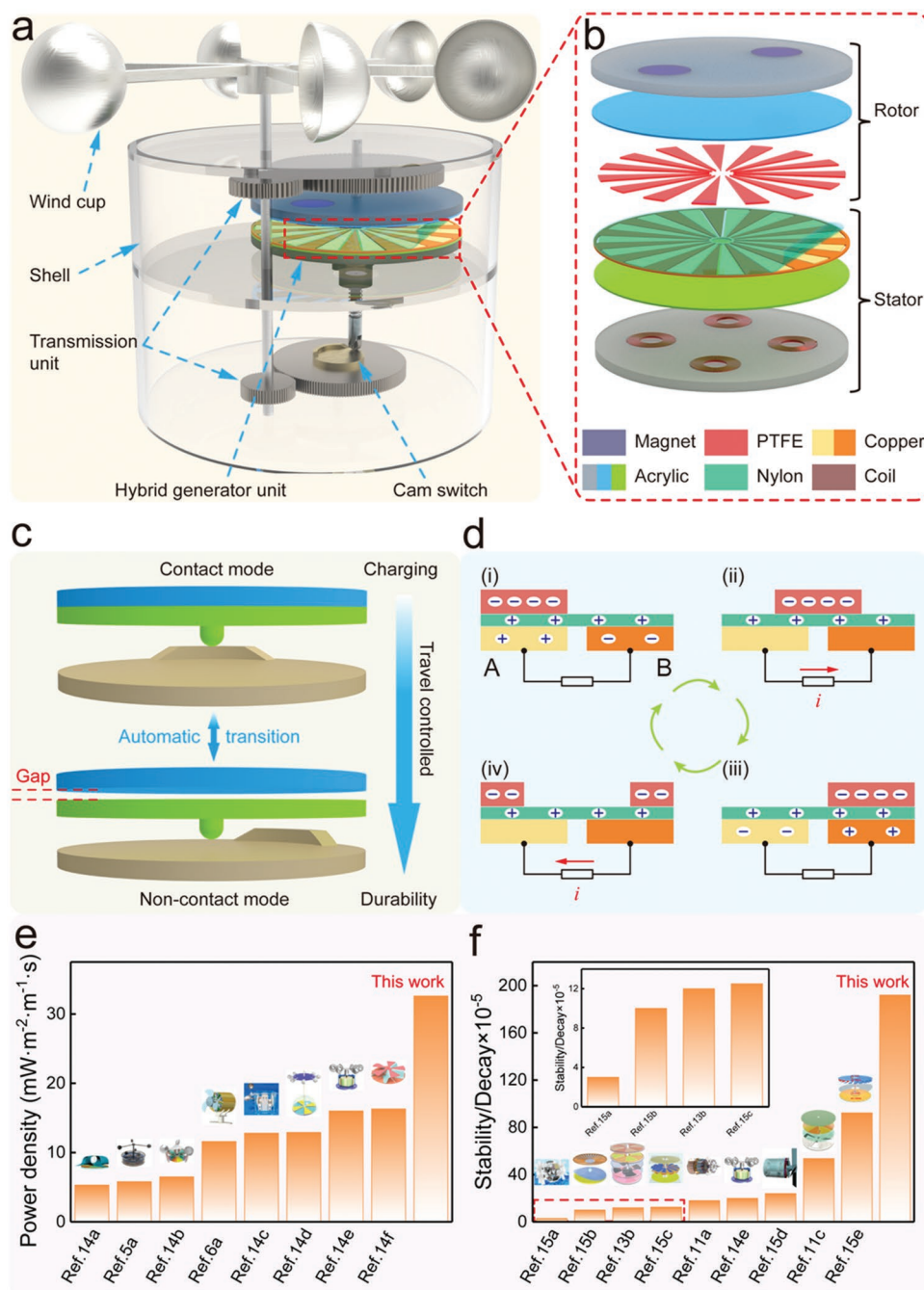
Figure 1. Schematic structure and working principle of the breeze-driven hybrid nanogenerator device. a) The whole structure of the hybrid device containing the TC-TENG and EMG. b) Enlarged view of the hybrid generator unit. c) Illustration of the automatic working mode transition. d) Schematic working principle of the TENG working in the freestanding mode. e) Comparison of the peak power density per unit wind speed of the TC-TENG with other related devices. f) Comparison of the device stability of this work with that reported by others.

The power density, as one of the most important basic parameters, is regarded as an indicator to assess the output performance of the TENG. Besides, the power density has almost a linear relationship with the wind speed, according to previous studies[5a,6a] and Figure S8, Supporting Information. Therefore, a normalized quantitative index of power density at different wind speeds (power density/wind speed) is proposed to better horizontally assess the output performance of the TENG, as shown in Figure 1e. Obviously, based on the structural optimization, the power density per unit wind speed of the TC-TENG is 32.6 mW m^{-2} m^{-1} s, which is twice that of previous related work.[5a,6a,14] On the other hand, the wear of the triboelectric material has always been a vital problem in the long-term work of the TENG for wind energy harvesting in the natural environment. Compared to previous works,[11a,c,13b,14e,15] the TC-TENG shows excellent long-term running stability, with

**ADVANCED
SCIENCE NEWS**
www.advancedsciencenews.com

**ADVANCED
FUNCTIONAL
MATERIALS**
www.afm-journal.de

only a 10% drop in performance over 1.92 million continuous cycles, and the stability/decay value is at least twice (Figure 1f). Therefore, benefiting from the improvement of the TC-TENG performance, this work offers a potential solution for the effective and stable collection of breeze energy.

2.2. Performance Optimization of the Hybrid Device

To ensure the operation of the hybrid nanogenerator device in a breezy environment and optimize its output performance, we investigated the operating torque and output performance of the device under stable lab-controlled conditions. The operating torque includes the contact torque of the rotor and stator, and the inertia torque due to the mass of the rotating part (including the wind cup and the magnets in the EMG part). A standardized experimental platform was established to meet the experimental requirements, as schematically shown in **Figure 2**a. The TENG-EMG device is fixed to the horizontal *XY*-direction platform (accuracy of 0.1 mm), which can fine-tune the distance between the device and torque sensor for accurately measuring the contact torque between the rotor and the stator. Meanwhile, the stepper motor driving the whole system and the torque sensor (accuracy of 0.001 N·m), which monitors the torque in real-time, are fixed to the vertical *XZ*-direction platform (accuracy of 0.1 mm). The rotating speed was set to be 100 rpm as it is close to the wind speed of 3 m s^{-1} in a natural environment.

First, the influence of different negative triboelectric materials on the output voltage of the TENG part was investigated at 100 rpm and an operating torque of 0.05 N m (Figure 2b). The results indicate that the TENG with the FEP film has the best output performance when using acrylic as the base material (left side of Figure 2b). However, in subsequent long-term wear resistance tests, the FEP film was more prone to warping and peeling than the PTFE film, which was finally chosen to be used in the device. In addition, the effect of the base material on the output of the TENG part was further studied (right side of Figure 2b), indicating that using the acrylic base can get an increase of 40% in the voltage, mainly because of the positive charges on its surface.

Besides the material effect, we also explored the effects of the cam parameters on the TENG outputs. The contact torque of the rotor and the stator and output voltage, with respect to the height of the convex plate, is shown in Figure 2c. As can be seen, at the contact mode, the increase of the convex plate height causes the increased output voltage of the TC-TENG and contact torque. That is because the convex plate height determines the distance between the stator and the rotor and the contact force. The increase of contact torque may severely limit the viability of the whole device under breezy conditions, as the device requires more driving force to operate. In contrast, in the non-contact mode, the output voltage decreases with increasing the convex plate height, ascribed to the increase of the gap between the stator and rotor. When the gap increases to 2 mm, the voltage is decreased by 90%.

Subsequently, the length ratio of convex plate in the cam, which can change the ratio of operating time for the contact and non-contact modes during a switching cycle, was tuned to optimize the output performance of the TENG part.

As shown in Figure 2d, there is a significant increase in the root-mean-square value of output voltage (V_{RMS}) as the convex plate length ratio increases, due to the increased operating time of the contact mode. However, the negative work done by the contact torque (E_{Torque}) increases markedly, which could cause a decrease in the energy conversion efficiency of the TENG part. For effective operation in a breezy environment, a balance needs to be achieved between the energy conversion efficiency and electric outputs. As a result, the optimal height and length ratio of the convex plate were finalized as 0.4 mm and 30%, respectively.

Figure 2e shows the inertia torque caused by different wind cup diameters, as a resistance term defined as the product of the force and arm. The whole inertia torque T_{wi} produced by six wind cups with the same diameter increases with increasing the diameter of wind cup, because of the increased mass of wind cups. The driving torque T_d generated by individual wind cup also follows a similar trend due to the increase in the windward area of the wind cup. Moreover, the inertia torque of the magnet in the EMG part was found to increase with the increase of the magnet mass, as well as the output voltage of the EMG, as shown in Figure 2f. The magnetic field intensities corresponding to different magnet masses are shown in Figure S2 of Supporting Information. Hence, the wind cup diameter and magnet mass were chosen to be 120 mm and 93 g to keep an appropriate inertia torque. After that, the output performance of the device was tested, showing an open-circuit voltage of 390 V, a transferred charge of 180 nC, and an operating torque of 0.05 N m for the TENG part (Figure 2g).

Moreover, the long-term durability of the TC-TENG was evaluated by comparing it with the contact-mode TENG, as presented in Figure 2h. The normalized transferred charge of the TC-TENG exhibits outstanding electrical stability compared with the constant contact modes. For example, after continuous operation for 80 h at 100 rpm, the transferred charge still maintains 90% of the initial value, while it decays sharply by 50% after 5 h at the low-speed contact mode, and by 60% after 2 h at the high-speed contact mode (500 rpm). For comparison, Figure 2i shows the optical microscope images of the PTFE and nylon surfaces in the automatic separation mode and low-speed contact mode (the results of high-speed contact mode are shown in Figure S3, Supporting Information). Strong mechanical wear can be observed on the surfaces of PTFE and nylon films at the constant contact mode, while the material wear is insignificant for the TC-TENG. In addition, we have further demonstrated the output performance of the device under various humidity conditions (Figure S4, Supporting Information). Clearly, because of the shell package, the humidity inside the shell hardly changes and the output performance of the non-contact mode TENG does not change significantly, regardless of the external ambient humidity, proving its viability in harsh environments.

2.3. Performance of the Hybrid Device under Breezy Conditions

To verify the feasibility of the TC-TENG for breeze energy harvesting, the performance characterizations and application demonstrations of a hybrid nanogenerator device were carried out by using a blower. **Figure 3**a and Figure S5, Supporting
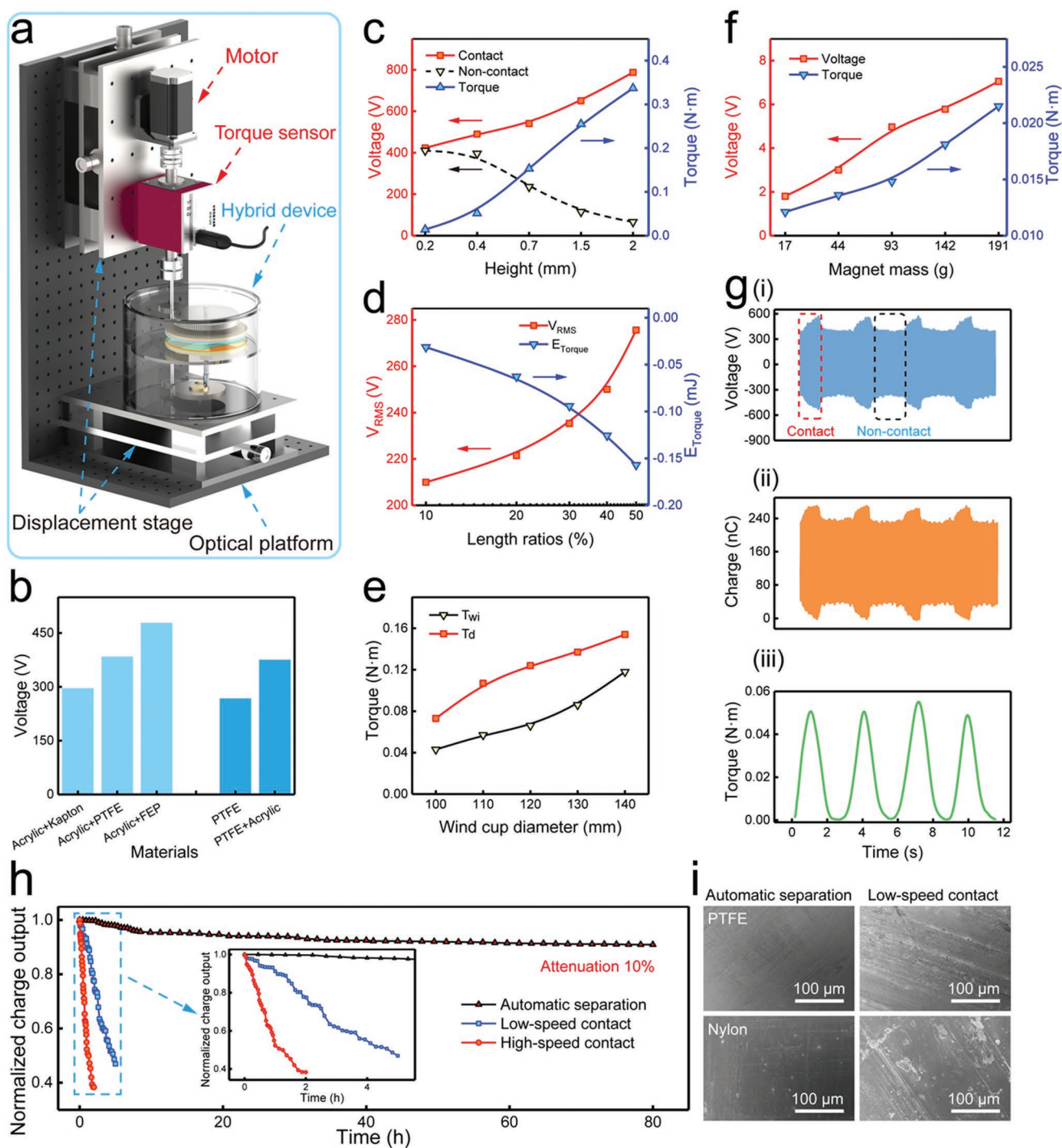
Figure 2. Influences of materials and structural parameters on the device performance. a) Schematic illustration of the whole experimental platform. b) Comparison of the output voltage of the TC-TENGs with various triboelectric materials at 100 rpm and 0.05 N m. c) Output voltage and contact torque at different convex plate heights. d) Root-mean-square voltage (V_{RMS}) and energy output of contact torque (E_{Torque}) for different length ratios of the convex plate. e) Whole inertia torque T_{wi} and driving torque T_d for various wind cup diameters. f) Output voltage and inertia torque of the EMG part with respect to the magnet mass. g) Output voltage, transferred charge, and operating torque of the TC-TENG at 300 rpm and 0.05 N m. h) Comparison of long-term durability for different operation modes. i) Optical microscope images of the PTFE and nylon surfaces at the automatic separation mode and low-speed contact mode for comparison.

Information show the output performance of the TENG part under various wind speeds. The output voltage does not change significantly, while the current increases gradually with the wind speed, reaching 12 µA at 7 m s. That is because, at a saturated transferred charge, the increase of wind speed reduces the time of each charge transfer cycle. Meanwhile, the dependence
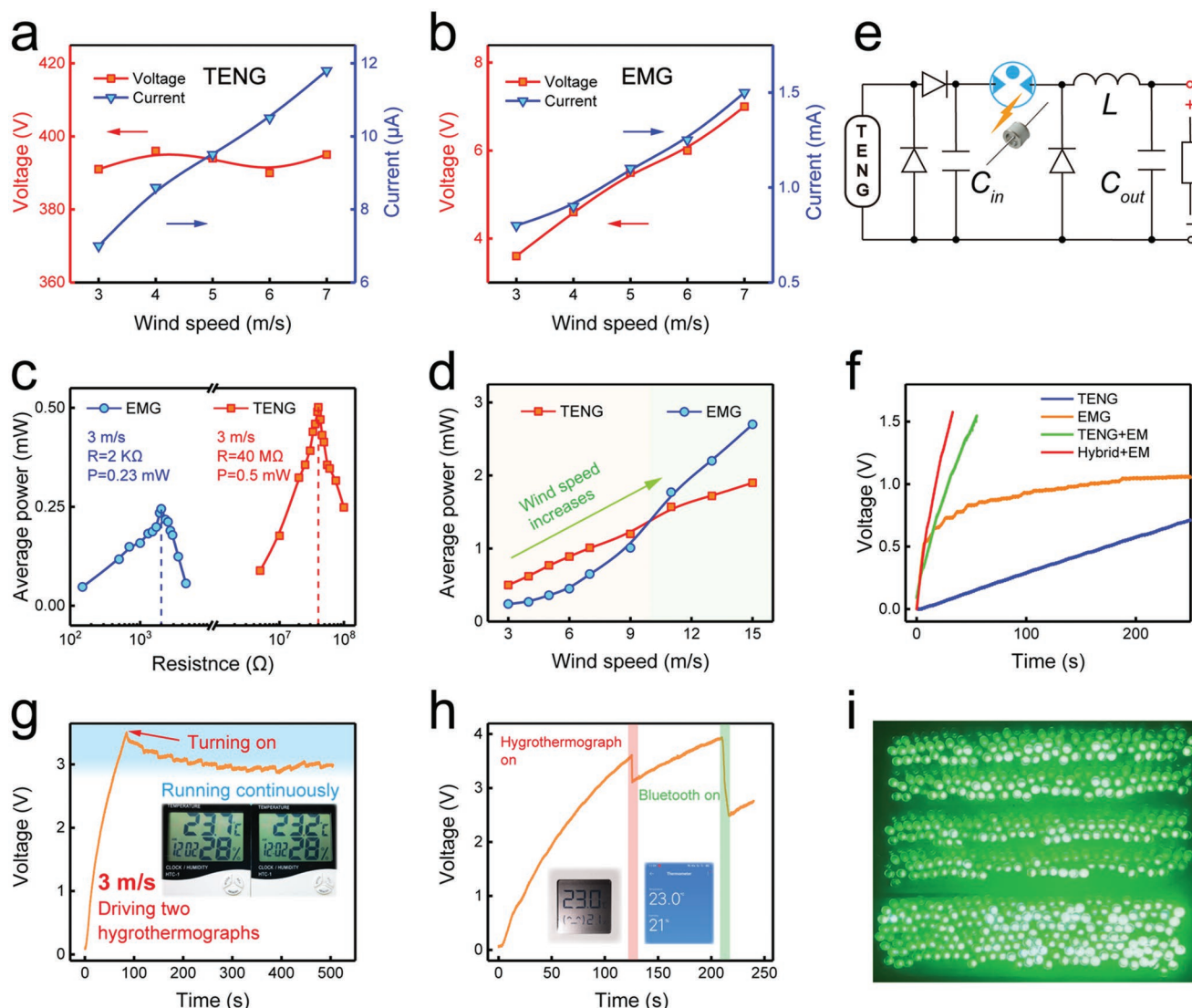
Figure 3. Performance characterizations and application demonstrations of the hybrid device. a) Output voltage and output current of the TENG part at different wind speeds. b) Output voltage and output current of the EMG part at various wind speeds. c) Average powers of the TENG part and EMG part at different load resistances under the wind speed of 3 m s⁻¹. d) Average powers for both the TENG part and EMG part under various wind speeds. e) Circuit diagram of the energy management for the TC-TENG. f) Comparison of the voltage profile on a 1 mF capacitor charged by the TENG, EMG, power-managed TENG, and power-managed hybrid device. g) Charging voltage on a 1 mF capacitor when powering two serial-connected hygrothermographs, driven by the TC-TENG at 3 m s⁻¹. h) Voltage profile on a commercial hygrothermograph with Bluetooth transmission function, running continuously powered by the TC-TENG. i) Photograph of 600 LEDs lighted up by the TC-TENG under the breeze triggering.

of output performance of the EMG part on the wind speed is shown in Figure 3b and Figure S6, Supporting Information. Different from the TENG, both the output voltage and current of the EMG unit increase with the wind speed almost linearly.

Moreover, the output power-resistance relationships for both the TENG part and EMG part at the wind speed of 3 m/s, corresponding to a breezy condition, were investigated, as shown in Figure 3c and Figure S7, Supporting Information. The average power of the TENG can be calculated by the following equation:

$$P_{ave} = \frac{\int_0^T I(t)^2 R \, dt}{T} \tag{1}$$

where $I(t)$ is the current across the resistor at the time t, R is the resistance, and T is the integration time. It can be seen that under the performed conditions, the average power and peak power (Figure S7, Supporting Information) of the TENG can reach the maximum values of 0.5 and 1.2 mW, respectively, at the matched resistance of 40 MΩ. And at the matched resistance of 2 kΩ, a maximum average power of 0.23 mW and a maximum peak power of 0.55 mW can be delivered for the EMG (Figure 3c; Figure S7, Supporting Information), which are lower than those of the TENG. To quantitatively characterize the resistive load behaviors of TC-TENG and EMG over a wider wind speed range, the average powers for both were tested (Figure 3d) and the fitted relationship between average

power of the TC-TENG and wind speed is shown in Figure S8, Supporting Information. As wind speed increases, the average power of the TC-TENG increases rapidly, while the growth rate of EMG power rises slightly, and the two curves intersect at a wind speed of 9.8 m s^{-1}. It can be seen that the TENG part produces more power than the EMG part at low wind speeds. Although the EMG part can produce more average power at the wind speeds over the intersection, the wind speed is relatively rare in the natural environment.

In order to extract more energy from the TC-TENG at a low frequency, a matching energy management (EM) circuit is crucial. Different from the traditional management circuits that use mechanical switches,[16] the EM circuit we designed adopts a gas discharge tube (GDT) as a switch to realize the instantaneous release of the accumulated energy for faster charging to capacitors, as shown in Figure 3e. Here, a capacitor C_{in} is set to store the unstable electric energy generated by the TENG part. In addition, the comparison of the total energy in C_{in} after half-wave rectification and full-wave rectification during half output cycle of TENG was made, as shown in Figure S9, Supporting Information. It indicates that the half-wave rectification can effectively extract more energy from the random output of TENG, which is also consistent with previous research results.[17] Meanwhile, the effect of inductance in the energy management circuit was also tested, as illustrated in Figure S10, Supporting Information. According to the testing results, a matched capacitor C_{in} of 0.22 nF and an inductance L of 5.6 mH were selected for achieving optimal output performance. During the operation, when the voltage on the C_{in} is larger than the threshold voltage of the GDT switch, the GDT switch is turned on, so that the energy stored in the capacitor C_{in} is instantly released to the inductor. After that, the GDT will be turned off, and the energy in the inductor will continue to charge the capacitor through the closed-loop circuit at the back end, forming a complete energy cycle. Then the charging performance of the hybrid nanogenerator device, integrated with the matched EM circuit, was measured at the wind speed of 3 m s^{-1}, as shown in Figure 3f. Compared to the TENG, EMG, and power-managed TENG, the power-managed hybrid nanogenerator can realize a faster-charging speed for a 1 mF capacitor. The EM part increases the charging speed by a factor of 14, where the voltage on the 1 mF capacitor can be raised to 1.5 V within 38 s.

For application demonstrations, the breeze-driven hybrid device was applied to power the temperature and humidity sensors for environmental monitoring, at the wind speed of 3 m s^{-1}. Figure 3g shows the measured voltage on the stored capacitor (1 mF) when powering two serial-connected hygrothermographs, which can operate stably and continuously. The whole running process is recorded in Video S1, Supporting Information. Meanwhile, a commercial hygrothermograph with Bluetooth transmission function, powered by the hybrid device, can successfully transmit environmental information to a mobile phone, as shown in Figure 3h. By means of a temporary energy storage capacitor of 1 mF, the temperature and humidity data can be displayed in real-time in the APP interface (Video S2, Supporting Information). Finally, 600 light-emitting diodes (LEDs) are also directly lighted up by the hybrid device under the same experimental conditions (Figure 3i and Video S3, Supporting Information).

2.4. Construction of Self-Powered Environmental Monitoring System

Based on the strong wind energy harvesting capability of the hybrid device, a closed-looped, self-powered environmental monitoring system in a breezy environment can be developed. The wireless sensor node is powered by the breeze-driven hybrid device integrated with the EM circuit, illustrating the possibility of using the hybrid device for long-term, uninhabited natural environmental monitoring, as shown in **Figure 4**a. In order to realize long-distance and stable wireless transmission, an ultra-low-power wireless sensor node for environmental monitoring was designed based on the Zigbee technology, as shown in Figure S11, Supporting Information. In a simulated breezy environment generated by the blower, through harvesting the wind energy, the hybrid device can drive the wireless sensor node to transmit environmental data to the receiver located as far as 100 m. Subsequently, the computer or mobile terminal records and processes the environmental information received by the receiver. These processes are carried out fully autonomously, without human intervention.

To demonstrate the feasibility of the whole integrated system, we conducted a long-running experiment of 2 h on the whole system, as shown in Figure 4b. When the capacitor of 1 mF is charged from 0 to 4 V by the hybrid device under the wind speed of 3 m s^{-1}, the wireless sensor node for environmental monitoring is activated. The enlarged voltage profile on the sensor node can be found in Figure 4b(i). Once the node has been activated, ambient temperature and humidity data are detected and transmitted to the receiver, and when the voltage drops to 3 V, the node goes to sleep. The whole system transmits the environmental data to the receiver every 43 s. The enlarged voltage curve after the operation of 2 h is shown in Figure 4b(ii). Clearly, after 2 h, the operating and sleeping voltages of the node do not fluctuate significantly, proving that the whole system can work stably and continuously for a long time in a breezy environment. The operating current of the node is 20 mA as shown in Figure 4b(iii). Figure 4c shows the temperature and humidity data received near the node during 2 h. Once the node detects that the ambient temperature or humidity exceeds a preset threshold, it can also send an alarm message at once, as shown in Figure 4d and Video S4, Supporting Information. Meanwhile, the voltage curve and the detailed values of temperature and humidity are recorded in Figure S12 and Table S1, Supporting Information, respectively. The self-powered environmental monitoring system, constructed based on the power-managed hybrid device under the breeze triggering, will find important application value in the fields of smart farming, smart grid, and forest/park fire warning.

3. Conclusion

In summary, we have developed a novel travel-controlled approach to reduce mechanical wear and improve the durability of hybrid TENG-EMG devices under breezy conditions. Through the rational design of the cam switch and gear train, the TC-TENG can autonomously realize the switching from the contact to non-contact working mode at the low wind speed
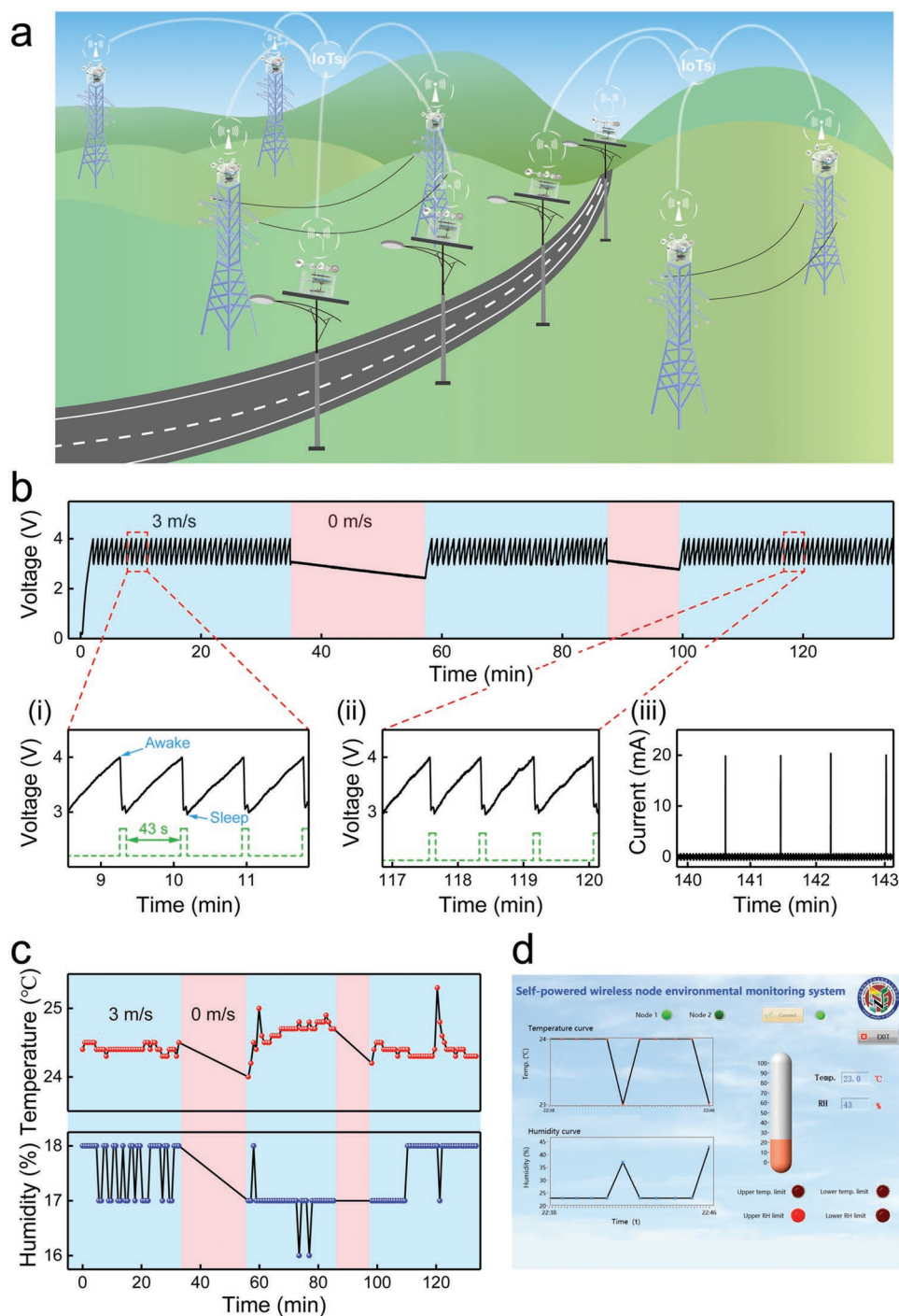
**ADVANCED
SCIENCE NEWS**

www.advancedsciencenews.com

**ADVANCED
FUNCTIONAL
MATERIALS**

www.afm-journal.de

Figure 4. Construction of self-powered environmental monitoring system based on the hybrid device through breeze energy harvesting. a) Sketch of the wireless self-powered environmental monitoring. b) Voltage profile of the whole environmental monitoring system running continuously for 2 h at the wind speed of 3 m s^{-1}, c) Received information on temperature and humidity with respect to the time. d) Display interface of the self-powered wireless sensor nodes for environmental monitoring.

of 3 m s^{-1}, and the power density per unit wind speed of the TC-TENG is doubled as compared with that of previous related works. During 80 h of continuous operation, its output performance decays <10%, which is significantly better than other works, indicating the enhanced device durability and extended working life. Importantly, based on the hybrid device integrated

with an EM circuit, a self-powered close-looped environmental monitoring and alarming system was developed, which can monitor the ambient environment steadily and continuously. The sensor node can be powered to wirelessly transmit temperature and humidity data autonomously to the receiver under breezy conditions. This work can provide a promising strategy

for improving the device durability at low wind speed, which can promote the applications of uninhabited environment monitoring and IoT technologies.

4. Experimental Section

Fabrication of the Hybrid Device Components: The hybrid device was composed of five parts: the wind cup, shell, transmission unit, cam switch, and hybrid generator unit. The wind cup and shell were made of acrylic, and the height and diameter of the shell were 220 and 200 mm, respectively.

The transmission unit consisted of a transmission shaft made by wire cutting and a gear train made by CNC machining. For the gears made with polyoxymethylene (POM), the tooth number and module of the pinion were 60 and 0.5, while those of the larger gear were 160 and 0.5. Besides, the cam switch was also CNC machined, with a cam diameter of 25 mm. The cam switch was machined using light-curing 3D printing technology, which had a diameter of 31 mm and a thickness of 3 mm.

The hybrid generator unit consisted of the rotor and stator. The rotor had an acrylic base by laser cutting, with a diameter of 125 mm and a thickness of 5 mm, respectively. The upper surface of the acrylic disk was symmetrically affixed to two circular neodymium magnets of equal mass with a diameter of 30 mm, thicknesses of 2 mm, 3 mm, and 5 mm, corresponding to the weights of 8.5 g, 13.5 g, and 24.5 g, respectively. The inertia torques of the EMG unit were measured for various magnet thicknesses. The lower surface of the acrylic disk was coated with 15 fan-shaped PTFE films with a central angle of 12° and a thickness of 50 μm. The material and dimensions of the stator are the same as those of the rotor. The upper surface of the stator had 30 copper electrodes with a central angle of 12° and a thickness of 20 μm, and the copper electrodes were coated with a 50 μm-thick nylon film. On the lower surface, 4 copper coils in series with an inner diameter of 4 mm, an outer diameter of 39 mm, a wire diameter of 0.1 mm, and a thickness of 4 mm, respectively, were applied.

Electrical Measurements and Characterizations of the Hybrid Device: The wind was produced by a commercial air blower (SHT-2.5A, POPULA, China), controlled by AC governors (ZADY6000X, CHNK, China), and the wind speed was tested by a digital anemometer (AS856, SMART SENSOR, China). The output signals of device were measured by an electrometer (6517B, Keithley, USA), and the output voltage of the TC-TENG was measured by combining a high-voltage probe (internal impedance: 1000 MΩ). The magnetic field intensity was tested by a digital teslameter (TD8620, Tunkia, China).

A commercial torque sensor (DYN-200, DAYSENSOR, China) was used to collect the torque data. When measuring the contact torque of the rotor and stator, the hybrid generation unit retains only the TENG part, i.e., the magnets and coils were removed. Different contact torques were tested by varying the height of the convex plate. The inertia torque of the wind cups was measured by fixing six equal-diameter wind cups to the drive shaft of the torque sensor via a bracket and driving the six cups at 100 rpm. The bracket diameter was 280 mm and the cup sizes were 100, 110, 120, 130, and 140 mm. The driving torque of the wind cup was measured by fixing a single wind cup to the drive shaft of the torque sensor, applying a jet of 3 m s⁻¹ directly to the cup, and measuring the torque at the moment when the cup is blown from rest. Similarly, the inertia torque of the EMG part was tested with only the rotor and magnets installed, and the data of the inertia torque at different magnet masses were obtained.

Supporting Information

Supporting Information is available from the Wiley Online Library or from the author.

Conflict of Interest

The authors declare no conflict of interest.

Data Availability Statement

The data that support the findings of this study are available from the corresponding author upon reasonable request.

[1] a) T. Zhao, M. Xu, X. Xiao, Y. Ma, Z. Li, Z. L. Wang, *Nano Energy* **2021**, *88*, 106381; b) Z. Lin, B. Zhang, Y. Xie, Z. Wu, J. Yang, Z. L. Wang, *Adv. Funct. Mater.* **2021**, *31*, 2105237; c) D. Liu, B. Chen, J. An, C. Li, G. Liu, J. Shao, W. Tang, C. Zhang, Z. L. Wang, *Nano Energy* **2020**, *73*, 104819.

[2] a) M. Yin, X. Lu, G. Qiao, Y. Xu, Y. Wang, T. Cheng, Z. L. Wang, *Adv. Energy Mater.* **2020**, *10*, 2000627; b) Q. Tang, M.-H. Yeh, G. Liu, S. Li, J. Chen, Y. Bai, L. Feng, M. Lai, K.-C. Ho, H. Guo, C. Hu, *Nano Energy* **2018**, *47*, 74.

[3] a) Z. L. Wang, T. Jiang, L. Xu, *Nano Energy* **2017**, *39*, 9; b) X. Liang, T. Jiang, G. Liu, Y. Feng, C. Zhang, Z. L. Wang, *Energy Environ. Sci.* **2020**, *13*, 277; c) C. Zhang, L. Zhou, P. Cheng, D. Liu, C. Zhang, X. Li, S. Li, J. Wang, Z. L. Wang, *Adv. Energy Mater.* **2021**, *11*, 2003616; d) J. Wang, L. Pan, H. Guo, B. Zhang, R. Zhang, Z. Wu, C. Wu, L. Yang, R. Liao, Z. L. Wang, *Adv. Energy Mater.* **2019**, *9*, 1802892.

[4] a) Z. L. Wang, *Nano Energy* **2019**, *58*, 669; b) Y. Wang, E. Yang, T. Chen, J. Wang, Z. Hu, J. Mi, X. Pan, M. Xu, *Nano Energy* **2020**, *78*, 105279.

[5] a) S. Yong, J. Wang, L. Yang, H. Wang, H. Luo, R. Liao, Z. L. Wang, *Adv. Energy Mater.* **2021**, *11*, 2101194; b) C. Jung, D. Schindler, *Sustain. Energy Technol. Assess.* **2020**, *42*, 100852; c) C. de Castro, M. Mediavilla, L. J. Miguel, F. Frechoso, *Energy Policy* **2011**, *39*, 6677.

[6] a) X. Fu, S. Xu, Y. Gao, X. Zhang, G. Liu, H. Zhou, Y. Lv, C. Zhang, Z. L. Wang, *ACS Energy Lett.* **2021**, *6*, 2343; b) C. L. Archer, *J. Geophys. Res.* **2005**, *110*, D12110.

[7] a) C. Ye, K. Dong, J. An, J. Yi, X. Peng, C. Ning, Z. L. Wang, *ACS Energy Lett.* **2021**, 1443; b) L. W. Zhong, J. Song, *Science* **2006**, *312*, 242; c) Z. Ren, Z. Wang, Z. Liu, L. Wang, H. Guo, L. Li, S. Li, X. Chen, W. Tang, Z. L. Wang, *Adv. Energy Mater.* **2020**, *10*, 2001770; d) P. Lu, H. Pang, J. Ren, Y. Feng, J. An, X. Liang, T. Jiang, Z. L. Wang, *Adv. Mater. Technol.* **2021**, *6*, 2100496;

e) A. Ahmed, I. Hassan, T. Ibn-Mohammed, H. Mostafa, I. M. Reaney, L. S. C. Koh, J. Zu, Z. L. Wang, *Energy Environ. Sci.* **2017**, *10*, 653.

[8] a) Z. L. Wang, *Mater. Today* **2022**, *52*, 348; b) F.-R. Fan, Z.-Q. Tian, Z. L. Wang, *Nano Energy* **2012**, *1*, 328; c) Z. L. Wang, *Mater. Today* **2017**, *20*, 74.

[9] a) C. Zhang, W. Tang, C. Han, F. Fan, Z. L. Wang, *Adv. Mater.* **2014**, *26*, 3580; b) S. Xu, X. Fu, G. Liu, T. Tong, T. Bu, Z. L. Wang, C. Zhang, *iScience* **2021**, *24*, 102318.

[10] a) P. Rui, W. Zhang, P. Wang, *ACS Nano* **2021**, *15*, 6949; b) Y. Feng, T. Jiang, X. Liang, J. An, Z. L. Wang, *Appl. Phys. Rev.* **2020**, *7*, 021401; c) J. Han, Y. Feng, P. Chen, X. Liang, H. Pang, T. Jiang, Z. L. Wang, *Adv. Funct. Mater.* **2022**, *32*, 2108580.

[11] a) B. Zhao, Z. Li, X. Liao, L. Qiao, Y. Li, S. Dong, Z. Zhang, B. Zhang, *Nano Energy* **2021**, *89*, 106381; b) Y. Cho, K. Lee, S. Park, S. Ahn, W. Kim, J. Kim, S. Park, J. Sun, C. Jung, J. Chung, M. Chang, D. Choi, J.-J. Park, *Nano Energy* **2019**, *61*, 370; c) P. Chen, J. An, S. Shu, R. Cheng, J. Nie, T. Jiang, Z. L. Wang, *Adv. Energy Mater.* **2021**, *11*, 2003066.

[12] a) L. Lin, Y. Xie, S. Niu, S. Wang, P.-K. Yang, Z. L. Wang, *ACS Nano* **2015**, *9*, 922; b) H. Guo, J. Chen, M.-H. Yeh, X. Fan, Z. Wen, Z. Li, C. Hu, Z. L. Wang, *ACS Nano* **2015**, *9*, 5577; c) M.-H. Yeh, H. Guo, L. Lin, Z. Wen, Z. Li, C. Hu, Z. L. Wang, *Adv. Funct. Mater.* **2016**, *26*, 1054; d) T. Jiang, H. Pang, J. An, P. Lu, Y. Feng, X. Liang, W. Zhong, Z. L. Wang, *Adv. Energy Mater.* **2020**, *10*, 2000064; e) Z. Lin, B. Zhang, H. Zou, Z. Wu, H. Guo, Y. Zhang, J. Yang, Z. L. Wang, *Nano Energy* **2020**, *68*, 104378.

[13] a) J. Chen, H. Guo, C. Hu, Z. L. Wang, *Adv. Energy Mater.* **2020**, *10*, 2000886; b) S. Fu, W. He, Q. Tang, Z. Wang, W. Liu, Q. Li, C. Shan, L. Long, C. Hu, H. Liu, *Adv. Mater.* **2022**, *34*, 2105882.

[14] a) F. Wang, Z. Wang, Y. Zhou, C. Fu, F. Chen, Y. Zhang, H. Lu, Y. Wu, L. Chen, H. Zheng, *Nano Energy* **2020**, *78*, 105244; b) Y. Fang, T. Tang, Y. Li, C. Hou, F. Wen, Z. Yang, T. Chen, L. Sun, H. Liu, C. Lee, *iScience* **2021**, *24*, 102300; c) S. Liu, X. Li, Y. Wang, Y. Yang, L. Meng, T. Cheng, Z. L. Wang, *Nano Energy* **2021**, *83*, 105851; d) R. Xia, R. Zhang, Y. Jie, W. Zhao, X. Cao, Z. Wang, *Nano Energy* **2022**, *92*, 106685; e) X. Li, Y. Cao, X. Yu, Y. Xu, Y. Yang, S. Liu, T. Cheng, Z. L. Wang, *Appl. Energy* **2022**, *306*, 117977; f) C. Ye, K. Dong, J. An, J. Yi, X. Peng, C. Ning, Z. L. Wang, *ACS Energy Lett.* **2021**, *6*, 1443.

[15] a) H. Shao, P. Cheng, R. Chen, L. Xie, N. Sun, Q. Shen, X. Chen, Q. Zhu, Y. Zhang, Y. Liu, Z. Wen, X. Sun, *Nanomicro Lett* **2018**, *10*, 54; b) L. Zhou, D. Liu, Z. Zhao, S. Li, Y. Liu, L. Liu, Y. Gao, Z. L. Wang, J. Wang, *Adv. Energy Mater.* **2020**, *10*, 2002920; c) C. Zhang, Y. Liu, B. Zhang, O. Yang, W. Yuan, L. He, X. Wei, J. Wang, Z. L. Wang, *ACS Energy Lett.* **2021**, *6*, 1490; d) S. Li, S. Wang, Y. Zi, Z. Wen, L. Lin, G. Zhang, Z. L. Wang, *ACS Nano* **2015**, *9*, 7479; e) L. He, C. Zhang, B. Zhang, O. Yang, W. Yuan, L. Zhou, Z. Zhao, Z. Wu, J. Wang, Z. L. Wang, *ACS Nano* **2022**, *16*, 6244.

[16] Z. Wang, W. Liu, W. He, H. Guo, L. Long, Y. Xi, X. Wang, A. Liu, C. Hu, *Joule* **2021**, *5*, 441.

[17] S. Xu, L. Zhang, W. Ding, H. Guo, X. Wang, Z. L. Wang, *Nano Energy* **2019**, *66*, 104165.

2205710 (10 of 10)